Article

Obtaining Dissipative Kerr Solitons Deterministically Using Dual-Coupled Microresonators and a Simple Frequency Sweep

Andrés F. Calvo-Salcedo [1,*] , Neil Guerrero González [2] and Jose A. Jaramillo-Villegas [1,3]

1   Faculty of Engineering, Universidad Tecnológica de Pereira, Pereira 660003, Colombia
2   Faculty of Engineering and Architecture, Universidad Nacional de Colombia, Manizales 170002, Colombia
3   Laboratory for Research in Complex Systems, Menlo Park, CA 94104, USA
*   Correspondence: afcalvo@utp.edu.co

Abstract: The reliable generation of dissipative Kerr solitons (DKSs) enables applications in communications, metrology, optical clocks, and, more recently, artificial intelligence. We show how single DKS can be generated by Si_3N_4 dual-coupled microring resonators (DCMs). We modeled this coupled structure using the Lugiato–Lefever equation (LLE), including mode interactions in the dispersion profile. We also characterized the pump power and detuning parameter space for several mode interaction strengths and frequencies, and we found parameters for which a DKS could be deterministically obtained using a single, adiabatic frequency sweep with a constant pump power. We demonstrated deterministic single DKS generation for this path by simulating 200 times with different random noise inputs. This result paves the way for reliable, inexpensive, and deterministic single DKS generation in a simple setup.

Keywords: photonic; microring resonator; solitons

1. Introduction

Optical frequency combs (OFCs) can be generated using mode-locked lasers, electro-optical modulation of continuous-wave light, or integrated microresonators [1]. When these combs are produced in an integrated microresonator, they are called Kerr combs. Kerr combs have recently attracted a large amount of attention in the photonics research community; they have applications in areas such as communications, metrology, optical clocks, photonic radars, artificial intelligence, and quantum information [2–7]. Ensuring their reliability, robustness, and low cost is a key challenge.

Dissipative Kerr solitons (DKSs) are a special type of Kerr comb. DKS yield a series of discrete, equally spaced frequency lines in the output spectrum with a constant frequency offset. DKS generation can be performed using a single microring resonator (MRR) [1–3,8–10], defining paths in which the laser pump power and detuning are controlled [8,11]. To understand the dynamics of this structure, the different operating regions of the MRR in the parameter space $(\Delta, |S|^2)$ have been identified [8,12,13]. These regions correspond to cnoidal waves, including Turing rolls, perfect soliton crystals, and single solitons or single DKSs, as well as chaotic solitons, soliton molecules, and imperfect soliton crystals. Specifically, Jose Jaramillo et al. defined a deterministic path for single DKS generation in a Si_3N_4 MRR, based on the above-mentioned regional classification [8]. However, it is difficult to apply this technique in experiments because it requires the pump laser power and wavelength to be changed rapidly along a defined path.

Other approaches include thermal control, pulse-triggers, multiple laser pumps, and engineered spatial mode interactions, among others [1,2,14,15]. Although these approaches can generate solitons deterministically, they involve difficult and expensive experimental setups. In [16,17], it was demonstrated that mode-crossings due to spatial mode-interactions can allow deterministic single soliton generation in a single MRR. However, its approach

is conditioned by the structure's geometry, limiting achievable dispersion profile and constraining generation to the paths proposed by the study, which may not be optimal. One of the limitations of a single MRR is the inability to control mode interactions.

Recently, the use of dual-coupled microring resonators (DCM) has been proposed to facilitate single DKS generation [1,18–21]. This structure allows the formation of specific dispersion profiles that depend on the coupling of the auxiliary ring, thus facilitating the manufacturing and engineering of dispersion. DCM can be controlled to modify mode interactions and enlarge the region of the parameter space within which single solitons are stable, making them easier to obtain deterministically. Approaches such as [18–20,22–25] demonstrate mathematical models and the dynamics governing light propagation in this structure. While these approaches demonstrate the formation of a DKS, those structures do not control mode interaction. As a result, their impact is fixed and confined to the specific case studies.

Other work studies the stability and accessibility of DKSs in dual-coupled microresonators (DCMs) as the system parameters vary [26–29]. These approaches have led to mathematical frameworks that facilitate the study of frequency combs, in particular enabling the determination of parameter regimes (within which stationary waveforms such as Turing rolls and DKSs exist) and their stability. However, a drawback in these studies is that the models are exclusively designed for microresonators with normal dispersion, overlooking structures with anomalous dispersion. Additionally, the structures analyzed do not control the mode interaction, restricting the generalization of the obtained results. In [22], the authors propose a DCM to generate Turing rolls and single DKS. This structure considers anomalous dispersion and establishes a configuration of mode interactions, simplifying the acquisition of DKS based on the characterization of the parameter space $(\Delta, |S|^2)$. Additionally, they perform a stability analysis to identify regions in the parameter space in which DKSs are stable. However, the effect of mode interaction on DCM waveforms has not been thoroughly examined, nor their role in potentially limiting the accessibility of single DKS regions in the parameter space $(\Delta, |S|^2)$.

In this study, we numerically demonstrate the generation of a single DKS using a straightforward constant pump power with an adiabatic frequency sweep in a dual-ring Si_3N_4 structure, which is sufficiently slow that the state of the optical waveform is not affected by the rate of the sweep. In the DCM, the mode interactions are electrically controlled by a microheater in the auxiliary microring. We chose strength and frequency values that facilitated access to the soliton and avoided the chaotic region, based on these characterizations. Finally, we verified the deterministic generation of the DKS. This document has the following structure: First, we characterize within the parameter space $(\Delta, |S|^2)$ by fixing values of a and b. These values are experimentally chosen to generate DKSs in the lower region of the space, thereby circumventing the chaotic region. Next, we fixed values for four points of the $(\Delta, |S|^2)$ space and computed the probability of DKS generation for each point. These points are manually selected, considering the position facilitating the DKS generation with a constant $|S|^2$ and a sweep from blue to red. Following this, we select four sets of values for a and b where the DKSs generation probability is high and compute the parameter space for these configurations. This process allows us to visualize potential regions where DKSs may generate and to ascertain which configurations exhibit a more pronounced presence of these waves. Finally, we analyze the stability of each zone to determine if reliable generation of DKSs is feasible with these values.

2. Characterization of Pump Power and Detuning Parameter Space

To understand the influence of mode interactions in the DCM, we explored the operating regions in the parameter space $(\Delta, |S|^2)$. This study is necessary to identify the region where DKSs are generated. The characterization of the operating regions depends on applying the Lugiato–Lefever equation (LLE) [8,15]. The LLE serves as a mathematical framework to simulate and characterize the propagation of light within a microring resonator, modeled through the parameters of loss, coupling factor, and chromatic dispersion.

This framework is decisive when responding to input pump and damping parameter variations, providing a comprehensive tool for our analysis.

The DCM was modeled by incorporating an avoided mode crossing (AMX) in the LLE [17]. This AMX accounts for the optical effects caused by an auxiliary ring with a smaller radius within the main ring, as illustrated in Figure 1. The AMX on the physical device can be controlled using a microheater positioned on top of the auxiliary ring. The observed two peaks in the DCM (see Figure 1e) relative to the MRR result from mode interactions caused by AMX, where the resonance modes of the primary microring and the auxiliary ring couple strongly, manifesting as peaks in the spectral response. These peaks represent resonant states with altered mode density and enhanced light confinement, enabling specific dispersion profiles that support DKS generation. The LLE equation can be expressed as follows:

$$t_R \frac{\partial E(t,\tau)}{\partial t} = \left[-\alpha - i\delta_0 - iL\frac{\beta_2}{2}\frac{\partial^2}{\partial \tau^2} + i\gamma L|E|^2\right]E + \sqrt{\phi}E_{in} + i\sum_\mu \frac{a/2}{\mu-b}\tilde{E}_\mu(t)e^{i\mu\tau} \quad (1)$$

where $E(t,\tau)$ is the complex envelope of the total intracavity field, t is the time variable, τ is the fast time variable, t_R is the round-trip time, α is half of the total loss per round trip, δ_0 is the frequency detuning, L is the cavity length, β_2 is the second-order dispersion coefficient, γ is the Kerr coefficient, ϕ is the coupling coefficient between the waveguide and the microring resonator, E_{in} is the pump field, a and b are the strength and frequency of the mode interaction, respectively, and $\tilde{E}_\mu(t)$ is the Fourier transform, defined as

$$\tilde{E}_\mu(t) = \frac{1}{T_R}\int_0^{T_R} E(t,\tau)e^{-i\mu\tau}d\tau. \quad (2)$$

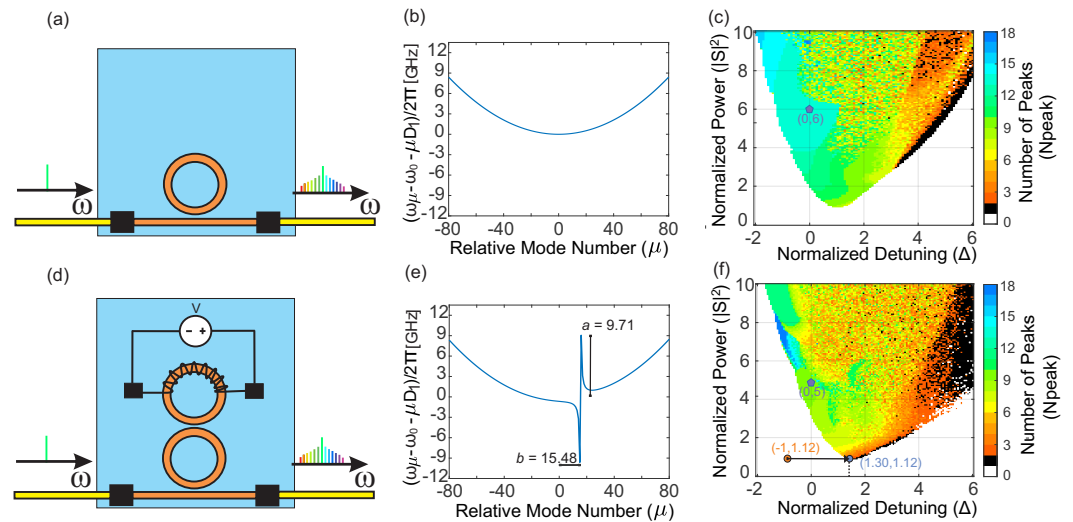**Figure 1.** (**a**) Microring resonator structure. (**b**) Dispersion profile of a single microring in the anomalous regime. (**c**) Npeak $(\Delta, |S|^2)$. (**d**) The structure of a two-coupled-microring resonator, with heater. (**e**) Dispersion with mode interactions (**f**) Npeak $(\Delta, |S|^2)$ with a two-coupled-microring structure. The blue point in (**f**) represents the initial point of the simulation.

The LLE equation incorporates AMX effects with the term

$$i\frac{1}{\alpha}\sum_\mu\left[\frac{\frac{a}{2}}{\mu-b}\widetilde{\psi}_\mu(T)e^{i\mu\theta}\right] \quad (3)$$

The parameter values for a and b were selected based on previous studies that validate this approach [16,30,31]. These studies highlight the role of AMX in facilitating DKS generation by lowering the threshold for soliton formation under certain dispersion conditions [30,31]. This incorporation of AMX into the LLE framework allows us to simu-

late and predict the influence of pump power and dissipation variations on modal dynamics and DKS formation. This approach is essential for understanding how device parameters impact DKS generation, providing insights for optimizing design in specific applications.

Equation (1) can be written in terms of three normalized parameters. One standard way to normalize Equation (1) is to let

$$\Delta = \frac{\delta_0}{\alpha} \qquad S = E_{\text{in}} \sqrt{\frac{\gamma L \phi}{\alpha^3}} \tag{4}$$

$$T = \frac{\alpha t}{t_R} \qquad \psi = \sqrt{\frac{\gamma L}{\alpha}} E \tag{5}$$

$$\beta = \frac{8\pi^3 R}{t_R^2 \alpha} \beta_2 = \frac{4\pi^2 L}{t_R^2 \alpha} \beta_2 \tag{6}$$

$$\theta = \frac{2\pi}{T_R} \tau \tag{7}$$

in which case Equation (1) becomes

$$\frac{\partial \psi}{\partial T} = -i \left[\frac{8\pi^3 R}{t_R^2} \frac{\beta_2}{2\alpha} \right] \frac{\partial^2 \psi}{\partial \theta^2} + i|\psi|^2 \psi - (i\Delta + 1)\psi + S + i \frac{1}{\alpha} \sum_\mu \left[\frac{a/2}{\mu - b} \widetilde{\psi}_\mu(T) e^{i\mu\theta} \right] \tag{8}$$

where

$$\tilde{\psi}_\mu(T) = \frac{1}{2\pi} \int_0^{2\pi} \psi(T, \theta) e^{-i\mu\theta} d\theta \tag{9}$$

To solve this equation numerically, we used the split-step Fourier method. Note that the normalized parameter definitions proposed in Equation (8) facilitate our analyses in a more general framework, and allow for comparison with other methods presented in the literature [8,15]. To perform the simulation of the LLE model, we used the same parameters as in [8] which correspond to a Si_3N_4 structure. The parameters used were a main radius of 100 μm, $t_R = 1/226$ GHz, $\beta_2 = -4.7 \times 10^{-26}$ [$s^2 m^{-1}$], $\alpha = 1.61 \times 10^{-3}$, $\gamma = 1.09$ [$W^{-1}m^{-1}$], $L = 2\pi \times 100$ [μm], and $\theta = 6.4 \times 10^{-4}$. The parameters chosen in the LLE model are founded on experimentally validated values from real physical devices [8,32,33]. Additionally, we replicated real conditions in the simulation by initializing the intracavity field with Gaussian noise, set at a standard deviation $\sigma_{\text{noise}} = 10^{-9}$ [$W^{1/2}$], which is added at each iteration. This approach ensures that our simulations are closely aligned with practical implementations, accurately reflecting the behavior of physical photonic systems. Due to the complexity and computational cost, thermal shift was not included in the model.

Additionally, we set the pump power for the single MRR at a detuning ($\Delta = 0$) and a pump power of $|P_{\text{in}}|^2 = 6$ (57.1 mW), ensuring a well-defined behavior in the cnoidal wave region. Similarly, for the DCM, we tuned the pump power at a detuning ($\Delta = 0$) and $|P_{\text{in}}|^2 = 5$ (47.6 mW). These values were chosen because this is the starting point for obtaining stable solitons [8]. Then, a single step jump was made to a point in the parameter space ($\Delta, |S|^2$) and maintained for 1.5 μs ($\approx 1310\, t_{\text{ph}}$). We chose a configuration (a, b) that shifted the single soliton region to be accessible from the blue side of the comb generation region in the parameter space ($\Delta, |S|^2$). These values are $a = 2\pi \times 9.71$ [GHz] and $b = 15.48$, in which we observed the shift of DKS region taking into account that the should potentially be replicated in experiments. To emphasize, generating a mode interaction strength greater than $a = 2\pi \times 10$ [GHz] could be physically unfeasible in chip design because achieving this interaction with the geometric designs proposed in the literature poses a challenge [1,34]. Hence, exploring values below this threshold is warranted to align with experimental limitations.

Figure 1c,f show the simulation results for a single MRR and DCM, respectively. In these simulations, we show the number of peaks in the time domain for each endpoint

$(\Delta, |S|^2)$ after 3 μs. In the first simulation with a single ring (see Figure 1c), we emphasize the presence of the thin black DKS region on the right side of the comb generation zone. The location of this region in the parameter space poses challenges for accessing DKS. The difficulty occurs because the path must avoid the chaotic zone, requiring the proposal of a non-linear route. Next, we simulated the DCM by introducing the mode interaction with the parameters (a, b) we previously proposed. The shift of the DKS area to the left and bottom of the region where combs are generated is apparent. This new position of the single soliton region makes it accessible in a path at constant pump power and with detuning that sweeps directly from blue to red, as shown by the black arrow in Figure 1f.

We next study the impact of parameters (a, b) on the generation of single DKS. Instead of fixed values, we aim to identify effective combinations of a and b, increasing the probability of single DKS generation. This approach deepens system understanding and helps pattern recognition, aiding future research. To define (a, b), we analyzed the single DKS generation probability at four key points in the parameter space $(\Delta, |S|^2)$, producing an explicit function of a and b. The choice of these specific points was deliberate, guided by their strategic location below the chaotic region, avoiding crossing this region and making it accessible in a path with detuning that sweeps directly from blue to red. The probability calculation at each point was determined by systematically varying the (a, b) values across the specified ranges, where a ranged from 0 to $2\pi \times 18$ [GHz], and b ranged from 0 to 20. The number of iterations used in the probability calculation was 30 simulations, introducing variability in the initial field and in the integration path through Gaussian noise with $\sigma_{\text{noise}} = 10^{-9} [\text{W}^{1/2}]$.

Figure 2 presents the probability of single DKS generation as a function of different parameter values (a, b), exploring these variations at the four specified points. Notably, various configurations of (a, b) exist, enabling reliable single DKS generation. However, many of these configurations are unattainable in a physics device, so we prefer those with a value of a less than $a = 2\pi \times 10$ [GHz]. To maximize the generation probability, we have deliberately chosen specific values corresponding to the regions of the graph marked with red, magenta, green, and black rectangles. These values, proven to be potential in terms of DKS generation, are as follows: $(a_1 = 2\pi \times 7.71$ [GHz], $b_1 = 10.56)$, $(a_2 = 2\pi \times 8.67$ [GHz], $b_2 = 16.32)$, $(a_3 = 2\pi \times 9.71$ [GHz], $b_3 = 13.44)$, $(a_4 = 2\pi \times 15.71$ [GHz], $b_4 = 15.48)$. This selection is based on the maximum generation probability associated with the chosen points, aiming to ensure reliable device performance under consideration.
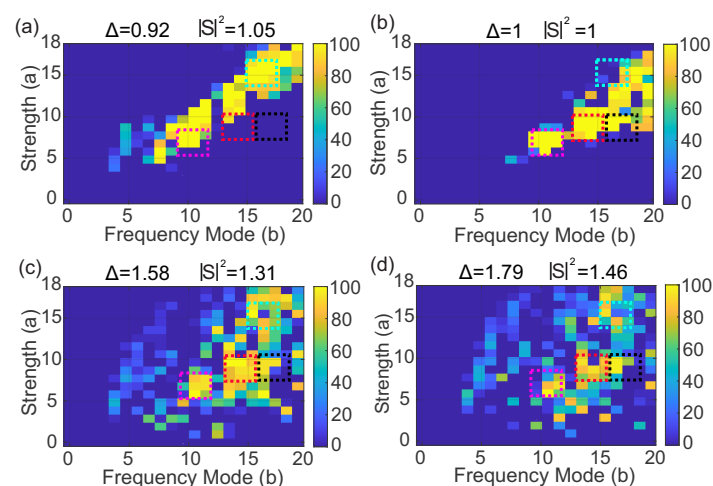

Figure 2. (**a**) DKS magenta, green, and black rectangles probability generation for the point ($\Delta_1 = 0.92$, $|S_1|^2 = 1.05$). (**b**) DKS probability generation for the point ($\Delta_2 = 1, |S_2|^2 = 1$). (**c**) DKS probability generation for the point ($\Delta_3 = 1.58, |S_3|^2 = 1.31$). (**d**) DKS probability generation for the point ($\Delta_4 = 1.79, |S_4|^2 = 1.79$).

Figure 3 displays the parameter space $(\Delta, |S|^2)$ for the previously proposed parameters (a, b). It is important to note that all four figures show a single DKS area in the lower right part of the parameter space, highlighted in black. This signifies direct access to the soliton region without passing through the chaotic zone. In Figure 3d, the $(\Delta, |S|^2)$ parameter space exhibits a larger DKS region than with other choices of a and b (see Figure 3). However, the crossing strength is relatively large with $a = 2\pi \times 15.71$ [GHz], which may pose challenges in a physical experiment. Conversely, Figure 3a,c reveal a considerable area and offer potential values for a potential physical experiment. Although Figure 3 demonstrates the presence of single DKS in these spaces, verifying if the generation in these areas is deterministic is required. There is a possibility that a single DKS may not always be obtained, potentially compromising the reliability of the path. To verify path accuracy, it is necessary to conduct multiple simulations, as proposed in [17], and confirm the repeatability of the path under different noise conditions.
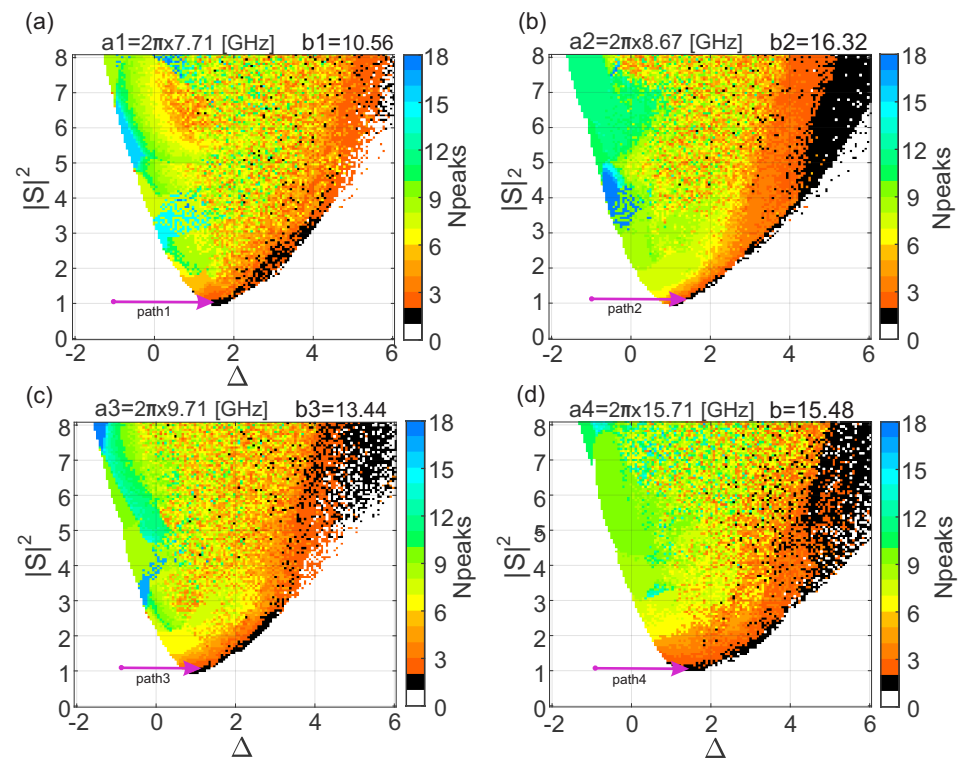

Figure 3. (**a**) Npeak $(\Delta, |S|^2)$ with the (a_1, b_1) parameters. (**b**) Npeak $(\Delta, |S|^2)$ with the (a_2, b_2) parameters. (**c**) Npeak $(\Delta, |S|^2)$ with the (a_3, b_3) parameters. (**d**) Npeak $(\Delta, |S|^2)$ with the (a_4, b_4) parameters.

3. Deterministic Single Soliton Generation

To demonstrate the deterministic access of single DKS in the four previously proposed configurations of a and b, we conducted 200 repetitions of the LLE simulation, employing distinct initial random fields for each setting. In the case of configuration (a_1, b_1), we maintained a constant normalized power $(|S|^2)$ of 1.04. The normalized detuning (Δ) was swept from -1 to 0.98 over a simulation period of 3 µs, as depicted in Figure 4a. For parameters (a_2, b_2), the magnitude $|S|^2$ was set to 1.1538, and the detuning Δ ranged from -1 to 1.5918. Similarly, for (a_3, b_3) parameters, $|S|^2$ equaled 1.08, with Δ spanning from -1 to 1.24. Finally, in the case of (a_4, b_4) parameters, $|S|^2$ was fixed at 1.09, and Δ varied from -1 to 0.93. The values of Δ and $|S|^2$ chosen for DKS generation along each path are determined by the trajectories indicated by the magenta arrows in Figure 3.
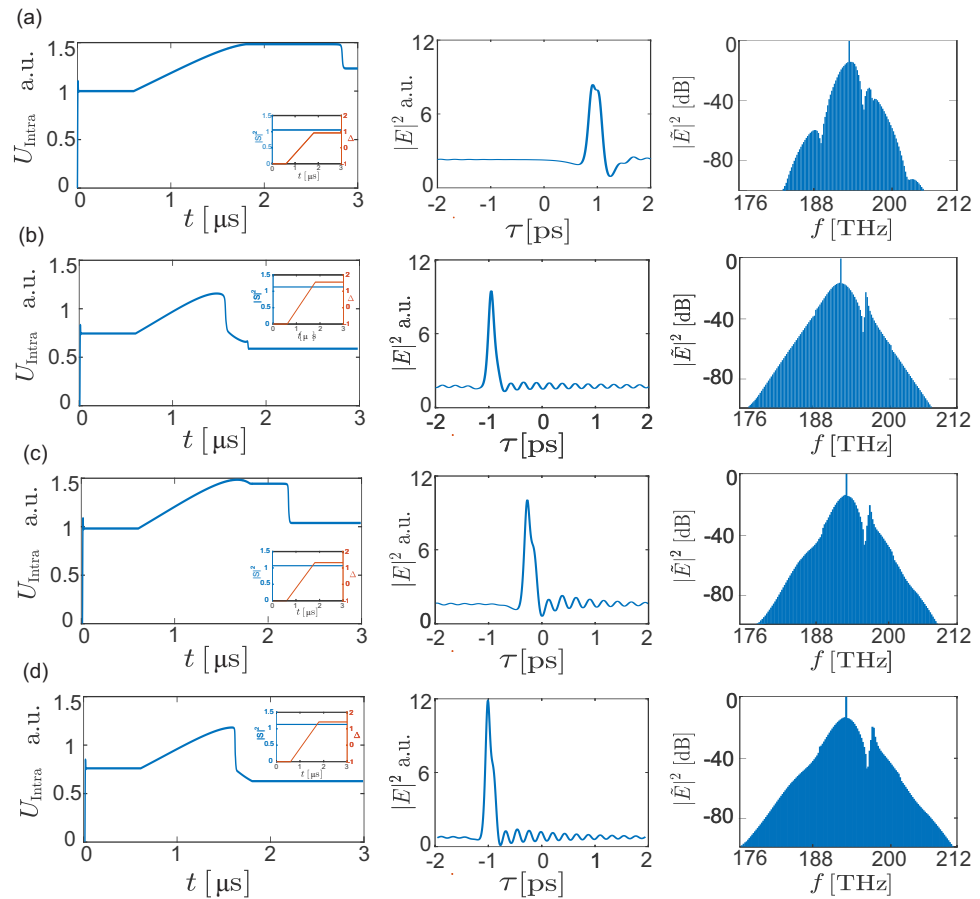
Figure 4. (**a**) OFC features for (a_1, b_1). (**b**) OFC features for (a_2, b_2), (**c**) OFC features for (a_3, b_3). (**d**) OFC features for (a_4, b_4). The features are the total intracavity energy—Uintra vs. slow time (**left**), optical intensity (**center**), optical spectrum (**right**).

We emphasize that these trajectories do not cross the chaotic region. Figure 4a–d show that we obtain a single DKS state; see the temporal shape (center) and spectrum (right). It is noteworthy that when the value of a is $a = 2\pi \times 7.71$ [GHz], the contour of the spectrum deviates from the a hyperbolic-secant shape. However, increasing a causes this shape to align more closely with the sech(x) shape. Note that configuration (a_1, b_1) does not conform to the sech(x) shape, unlike the other configurations. Figure 4a–d show that U_{intra} remains stable and noise-free along the selected paths, supporting controlled DKS generation. The absence of abrupt fluctuations confirms that the trajectory avoids chaotic regions, essential for stability. Additionally, the convergence of U_{intra} to a constant value indicates that the DKS reaches a stable configuration, which is crucial for maintaining coherence in different applications.

Figure 5 shows the number of peaks (N_{peaks}) for the 200 simulations in the four proposed a and b configurations. We obtained in a single peak in all the realizations, indicating that a single DKS was always generated, demonstrating that the paths are deterministic. Although these configurations enable the generation of a single DKS, these simulations do not demonstrate that the DKS is stable. For this reason, we perform a stability analysis.

To validate DKS generation under variations in the DCM caused by changes in aspect ratio and manufacturing tolerances, which affect the radius, loss, coupling coefficient, and dispersion of the device, we conducted a Monte Carlo simulation. In this simulation, we varied the radius, loss, coupling coefficient, and dispersion randomly within the ranges specified in Table 1. This approach allowed us to evaluate the robustness of DKS generation under realistic manufacturing fluctuations, ensuring reliable device performance within practical tolerance levels.
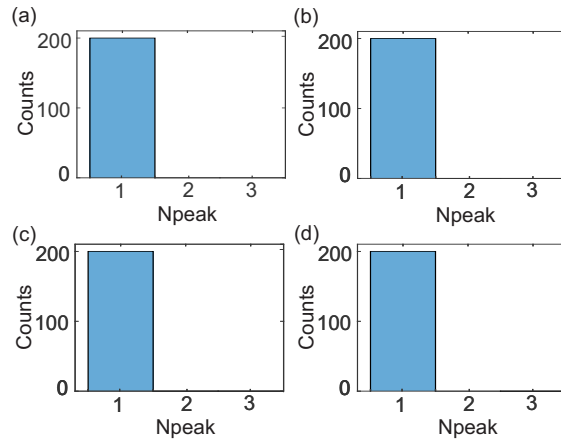
Figure 5. (**a**) Histogram of the number of peaks (Npeak) for 200 simulations for configuration (a_1, b_1), with different realizations of the initial noise. (**b**) Npeak histogram for configuration (a_2, b_2). (**c**) Npeak histogram for configuration (a_3, b_3). (**d**) Npeak histogram for configuration (a_4, b_4).

Table 1. Range of DCM intrinsic parameters.

Parameters	Range
radius	$[99, 103]$ $[\mu\mathrm{m}]$
α	$[1.594 \times 10^{-3}, 1.6113 \times 10^{-3}]$
θ	$[6.38 \times 10^{-4}, 6.49 \times 10^{-4}]$
β_2	$[-6.8 \times 10^{-26}, -3.8 \times 10^{-26}]$ $[\mathrm{s}^2\mathrm{m}^{-1}]$

As shown in Figure 6, we conducted 200 Monte Carlo iterations across the four paths defined in Figure 4, achieving DKS generation in 175 cases (Figure 6a), 130 cases (Figure 6b), 160 cases (Figure 6c), and 181 cases (Figure 6d). These results indicate a DKS generation probability exceeding 80% for Figure 6a,c,d and 65% for Figure 6b. While variations in the aspect ratio influenced the results, the method still showed robustness and adaptability to specific structural changes. Although DKS generation is not entirely deterministic, our approach can reliably be applied post-fabrication using precise parameters obtained after manufacturing, once the aspect ratio and device adjustments are confirmed. This characterization provides key parameters such as quality factor (Q), FSR, α, and θ, enabling precise DKS generation analysis and parameter mapping that ensures robustness and adaptability in fabricated devices.

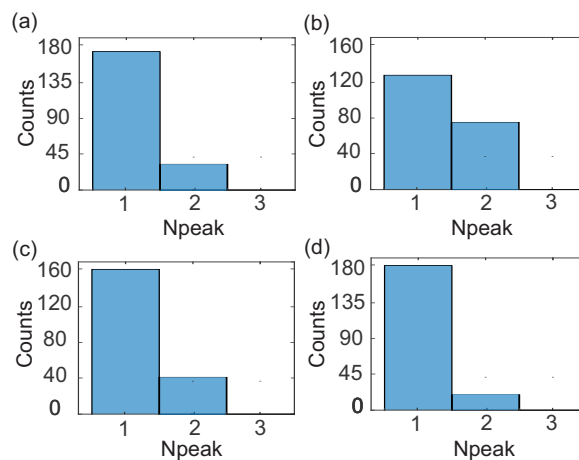**Figure 6.** (**a**) Monte Carlo histogram of the number of peaks (Npeak) for 200 simulations for configuration (a_1, b_1), with different intrinsic DCM parameters. (**b**) Npeak histogram for configuration (a_2, b_2). (**c**) Npeak histogram for configuration (a_3, b_3). (**d**) Npeak histogram for configuration (a_4, b_4).

4. Single DKS Stability Analysis

The selection of $|S|^2$ and (Δ) values is essential for achieving a stable DKS. Conducting a stability analysis is crucial, as it identifies the specific ranges of $|S|^2$ and (Δ) within which the DKS state can be maintained, thereby avoiding unintended frequency comb patterns or the absence of comb generation.

To analyze the stability region of the single DKS in the DCM, we propose a new method based on previous work [8,15]. Our proposed method first solves Equation (10) while allowing S or Δ to vary. To solve Equation (10), we employ the split-step Fourier evolution method, which yields a highly stable and stationary solution. To obtain this stable solution, we use the paths proposed above, which sweeps the detuning from Δ_1 to Δ_2 while keeping S constant. Subsequently, we jump to a final point in the range of $0 < |S|^2 < 2.5$ with a resolution of 0.025 in both parameters. At each point, we wait for 3 μs to evaluate the stability of DKS.

$$
\begin{aligned}
0 = &-i\left[\frac{8\pi^3 R}{t_R^2}\frac{\beta_2}{2\alpha}\right]\frac{\partial^2\psi}{\partial\theta^2} + i|\psi|^2\psi - (i\Delta+1)\psi + S \\
&+i\frac{1}{\alpha}\sum_\mu\left[\frac{a/2}{\mu-b}\widetilde{\psi}_\mu(T)e^{i\mu\theta}\right] + \left[\frac{t_s}{\alpha}\frac{2\pi}{T_R}\right]\frac{\partial\psi}{\partial\theta}
\end{aligned}
\tag{10}
$$

In parallel with solving Equation (10) to find the wave solutions, we determine their stability. We write

$$
\psi = \psi_0 + \Delta\psi \qquad \bar{\psi} = \psi_0^* + \bar{\Delta\psi}
\tag{11}
$$

where $\Delta\psi$ and $\bar{\Delta\psi}$ are perturbation of the solution ψ_0 and its complex conjugate ψ_0^*. The perturbations $\Delta\psi$ and $\bar{\Delta\psi}$ obey the linearized equation

$$
\frac{\partial\Delta\psi}{\partial T} = \mathcal{L}\Delta\psi
\tag{12}
$$

where

$$
\Delta\psi = \begin{bmatrix}\Delta\psi \\ \bar{\Delta\psi}\end{bmatrix}
\tag{13}
$$

and

$$
\mathcal{L} = \begin{bmatrix}\mathcal{L}_{11} & \mathcal{L}_{12} \\ \mathcal{L}_{21} & \mathcal{L}_{22}\end{bmatrix}
\tag{14}
$$

$$
\mathcal{L}_{11} = -i\left[\frac{8\pi^3 R\beta_2}{2\alpha t_R^2}\right]\frac{\partial^2}{\partial\theta^2} + 2i|\psi_0|^2 - i\Delta - 1 + \frac{i}{\alpha}F_t^{-1}\left[\frac{a/2}{\mu-b}\right]F_t + \frac{t_s 2\pi}{\alpha t_R}\frac{\partial}{\partial\theta}
\tag{15}
$$

$$
\mathcal{L}_{12} = i\psi_0^2 \qquad \mathcal{L}_{21} = -i(\psi_0^*)^2
\tag{16}
$$

$$
\mathcal{L}_{22} = i\left[\frac{8\pi^3 R\beta_2}{2\alpha t_R^2}\right]\frac{\partial^2}{\partial\theta^2} - 2i|\psi_0|^2 + i\Delta - 1 - \frac{i}{\alpha}F_t^{-1}\left[\frac{a/2}{\mu-b}\right]F_t + \frac{t_s 2\pi}{\alpha t_R}\frac{\partial}{\partial\theta}
\tag{17}
$$

The terms F_t and F_t^{-1} correspond to the Fourier transform and its inverse function. Those functions enable mathematical modeling, as these transforms have a matrix representation, and the term $\frac{a/2}{\mu-b}$ can be assigned to a diagonal matrix, resulting in a series of matrix operations of dimension $N \times N$ that operate on the solution vector $\psi(N \times 1)$. Next, We convert Equation (12) into an eigenvalue equation $(\mathcal{L} - \lambda I)\Delta\psi = 0$, where I is the identity operator, and we discretize this equation. We then proceed to computationally find the set of all eigenvalues λ_j of this equation. If any eigenvalues are positive in its real component, the solution $\frac{\partial\psi}{\partial T}$ is unstable for Δ and S values. t_s is a drift term introduced in the model because the avoided crossing introduces a slight drift in the solution, causing it to become non-stationary. To find t_s, we calculate the soliton centroid in two consecutive round trips, determining the θ difference between both to obtain this value. We repeat this process 30 times and calculate the average value. To evaluate the stability of single

DKS at each point, initially we determine the number of peaks by computing the optical intensity [8]. If the value of the number of peaks is one, it indicates that the wave may be stable. Otherwise, the wave will be unstable and will converge to a different type of wave. When the number of peaks is one, it indicates that the wave is a single DKS. Its stability is evaluated by computing the eigenvalue solution of the eigenvalue of the $\mathcal{L}$ matrix and validating that $\lambda_i < 0$. This process is necessary because a single soliton wave may not be inherently stable and can exhibit oscillations or breathing, which are considered unstable.

The red area in Figure 7 shows the regions where the single DKS is still stable at the end of the simulation for the four parameter sets (a, b) that we investigated proposed. This result shows that the deterministic generation of a single DKS is correlated with a greatly enhanced stable region. We also observe that the parameter space (a_1, b_1) exhibits a small stable region, suggesting that while a substantial number of single DKSs are produced, they are unstable, rendering them unreliable for deterministic generation (see Figure 7a). Furthermore, the other parameter spaces have a potential area for soliton generation (see Figure 7b–d). All the stable zones lie below the chaotic zone, which facilitates the generation of single DKS, as proposed in this research. Note that configuration (a_4, b_4) presents a value greater than $a = 2\pi \times 10$. This situation poses a challenge in the design and manufacturing process of DCM. Therefore, it is more feasible to utilize the configurations proposed in (a_2, b_2) and (a_3, b_3).
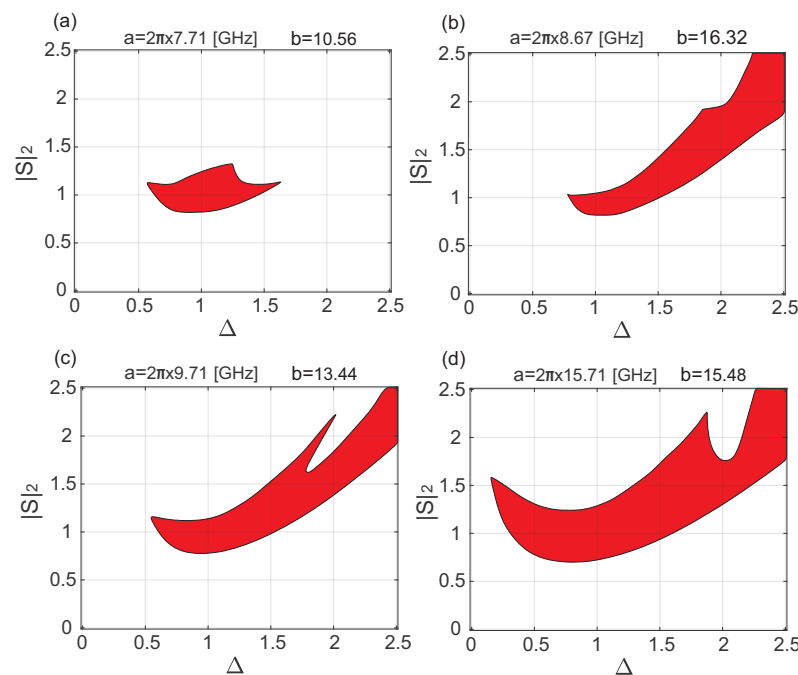

Figure 7. (**a**) Single DKS Stability region for (a_1, b_1). (**b**) DKS Stability region for (a_2, b_2), (**c**) DKS Stability region for (a_3, b_3). (**d**) DKS Stability region for (a_4, b_4).

5. Adiabatic DKS Generation

After confirming the stability of a single DKS generation, it is important to check if these paths can create a single DKS using an adiabatic trajectory. To validate those paths, we propose conducting the DKS generation using the same paths shown in Figure 4, extending the simulation time to 1 ms. Figure 8 presents the results for the proposed adiabatic paths. It is noteworthy that for all four configurations, we successfully achieved a single DKS, indicating the solutions' stability and ability to maintain their shape over time.
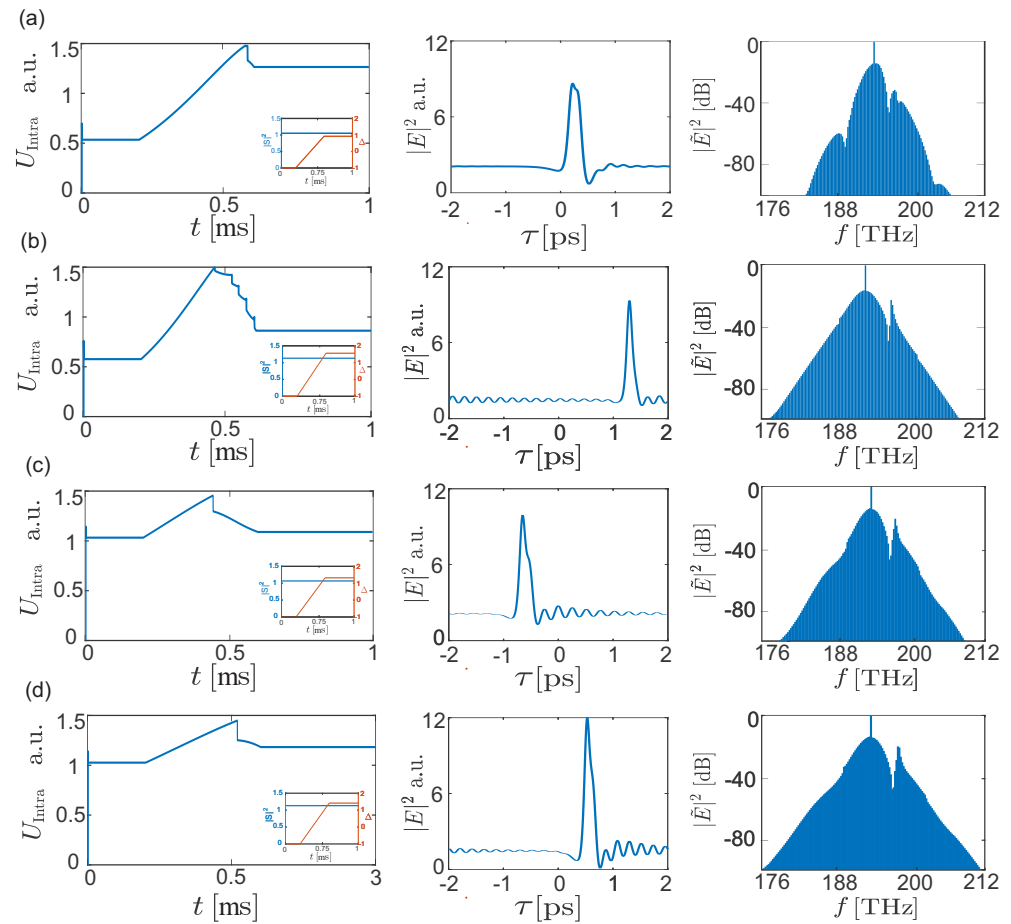
Figure 8. (**a**) DKS with adiabatic path and (a_1, b_1) parameters. (**b**) DKS with adiabatic path and (a_2, b_2) parameters. (**c**) DKS with adiabatic path and (a_3, b_3) parameters. (**d**) DKS with adiabatic path and (a_4, b_4) parameters.

6. Conclusions

This work presents a novel method for generating a single DKS using Si_3N_4 dual-coupled microring resonators with straightforward laser control. Furthermore, we demonstrate two dispersion profile that allow us to obtain an accessible single DKS region in the lower part of the parameter space $(\Delta, |S|^2)$. This change in the parameter space allows us to use a constant pump power with an adiabatic frequency sweep, and we obtain a direct path to the region in which a single DKS exists. The results presented in this article could help reduce the cost and complexity of generating a single DKS for practical applications and enable the use integrated optical frequency combs in mass produced devices. This work explores the influence of parameters a and b on the generation of DKS. The results illustrate that these parameters harbor the potential to produce deterministic and stable single DKS. Such insights contribute to a comprehensive understanding of this phenomenon in microresonators, facilitating advancements in their engineering and construction. To continue with this work, it is necessary to construct DCM with the dispersion profile proposed in this work (see Figure 3) and to perform an experimental validation of these results. Additionally, this physical design must consider an appropriate geometry to ensure a suitable aspect ratio, which is essential for achieving low losses.

Author Contributions: Methodology and implementation, A.F.C.-S.; conceptualization and investigation, N.G.G.; supervision, writing, and review, J.A.J.-V. All authors have read and agreed to the manuscript.

Conflicts of Interest: The authors declare that they have no known competing financial interests or personal relationships that could have appeared to influence the work reported in this paper.

References

1. Zhang, X.; Wang, C.; Cheng, Z.; Hu, C.; Ji, X.; Su, Y. Advances in resonator-based Kerr frequency combs with high conversion efficiencies. *npj Nanophotonics* **2024**, *1*, 26. [CrossRef]
2. Kippenberg, T.J.; Gaeta, A.L.; Lipson, M.; Gorodetsky, M.L. Dissipative Kerr solitons in optical microresonators. *Science* **2018**, *361*, eaan8083. [CrossRef]
3. Shen, Y.; Harris, N.C.; Skirlo, S.; Prabhu, M.; Baehr-Jones, T.; Hochberg, M.; Sun, X.; Zhao, S.; Larochelle, H.; Englund, D.; et al. Deep learning with coherent nanophotonic circuits. *Nat. Photonics* **2017**, *11*, 441–446. [CrossRef]
4. Tara, F.; Esther, B. 20 years of developments in optical frequency comb technology and applications. *Commun. Phys.* **2019**, *2*, 153. [CrossRef]
5. Weiner, A.M. Cavity solitons come of age. *Commun. Phys.* **2017**, *11*, 533–535. [CrossRef]
6. Jang, J.K.; Klenner, A.; Ji, X.; Okawachi, Y.; Lipson, M.; Gaeta, A.L. Synchronization of coupled optical microresonators. *Nat. Photonics* **2018**, *12*, 688–693. [CrossRef]
7. Maltese, G.; Amanti, M.I.; Appas, F.; Sinnl, G.; Lemaître, A.; Milman, P.; Baboux, F.; Ducci, S. Generation and symmetry control of quantum frequency combs. *npj Quantum Inf.* **2020**, *6*, 688–693. [CrossRef]
8. Jaramillo-Villegas, J.A.; Xue, X.; Wang, P.H.; Leaird, D.E.; Weiner, A.M. Deterministic single soliton generation and compression in microring resonators avoiding the chaotic region. *Opt. Express* **2015**, *23*, 9618–9626. [CrossRef]
9. Weng, H.; Afridi, A.A.; Li, J.; McDermott, M.; Tu, H.; Barry, L.P.; Lu, Q.; Guo, W.; Donegan, J.F. Dual-mode microresonators as straightforward access to octave-spanning dissipative Kerr solitons. *APL Photonics* **2022**, *7*, 066103. [CrossRef]
10. Wang, P.H.; Ferdous, F.; Miao, H.; Wang, J.; Leaird, D.E.; Srinivasan, K.; Chen, L.; Aksyuk, V.; Weiner, A.M. Observation of correlation between route to formation, coherence, noise, and communication performance of Kerr combs. *Opt. Express* **2012**, *20*, 29284–29295. [CrossRef]
11. Shen, B.; Chang, L.; Liu, J.; Wang, H.; Yang, Q.-F.; Xiang, C.; Wang, R.N.; He, J.; Liu, T.; Xie, W.; et al. Integrated turnkey soliton microcombs. *Nature* **2020**, *582*, 365–369. [CrossRef] [PubMed]
12. Chen, N.; Zhang, B.; Yang, H.; Lu, X.; He, S.; Hu, Y.; Chen, Y.; Zhang, X.; Xu, J. Stability analysis of generalized Lugiato-Lefever equation with lumped filter for Kerr soliton generation in anomalous dispersion regime. In Proceedings of the Asia Communications and Photonics Conference 2021, Shanghai China, 24–27 October 2021; Optica Publishing Group: Washington, DC, USA, 2021; p. T4A.187. [CrossRef]
13. Parra-Rivas, P.; Gomila, D.; Matías, M.A.; Coen, S.; Gelens, L. Dynamics of localized and patterned structures in the Lugiato-Lefever equation determine the stability and shape of optical frequency combs. *Phys. Rev. A* **2014**, *89*, 043813. [CrossRef]
14. Joshi, C.; Jang, J.K.; Luke, K.; Ji, X.; Miller, S.A.; Klenner, A.; Okawachi, Y.; Lipson, M.; Gaeta, A.L. Thermally controlled comb generation and soliton modelocking in microresonators. *Opt. Lett.* **2016**, *41*, 2565–2568. [CrossRef] [PubMed]
15. Qi, Z.; Wang, S.; Jaramillo-Villegas, J.; Qi, M.; Weiner, A.M.; D'Aguanno, G.; Carruthers, T.F.; Menyuk, C.R. Dissipative cnoidal waves (Turing rolls) and the soliton limit in microring resonators. *Optica* **2019**, *6*, 1220–1232. [CrossRef]
16. Bao, C.; Xuan, Y.; Leaird, D.E.; Wabnitz, S.; Qi, M.; Weiner, A.M. Spatial mode-interaction induced single soliton generation in microresonators. *Optica* **2017**, *4*, 1011–1015. [CrossRef]
17. Liu, H.; Wang, W.; Yang, J.; Yu, M.; Kwong, D.L.; Wong, C.W. Observation of deterministic double dissipative-Kerr-soliton generation with avoided mode crossing. *Phys. Rev. Res.* **2023**, *5*, 013172. [CrossRef]
18. Rebolledo-Salgado, I.; Quevedo-Galán, C.; Helgason, B.; Lööf, A.; Ye, Z.; Lei, F.; Schröder, J.; Zelan, M.; Torres-Company, V. Platicon dynamics in photonic molecules. *Commun. Phys.* **2023**, *6*, 303. [CrossRef]
19. Marti, L.; Vasco, J.P.; Savona, V. Slow-light enhanced frequency combs and dissipative Kerr solitons in silicon coupled-ring microresonators in the telecom band. *OSA Contin.* **2021**, *4*, 1247–1257. [CrossRef]
20. Komagata, K.; Tusnin, A.; Riemensberger, J.; Churaev, M.; Guo, H.; Tikan, A.; Kippenberg, T.J. Dissipative Kerr solitons in a photonic dimer on both sides of exceptional point. *Commun. Phys.* **2021**, *4*, 159. [CrossRef]

21. Wu, W.; Huang, D.; Cheng, Z.; Li, F.; Wai, P.K.A. Deterministic generation of Kerr soliton microcomb in coupled microresonators by a single-shot pulsed trigger. In Proceedings of the Fourteenth International Conference on Information Optics and Photonics (CIOP 2023), Xi'an, China, 7–10 August 2023; SPIE: Bellingham, WA, USA, 2023; Volume 12935, p. 129354G. [CrossRef]

22. Wu, Z.; Gao, Y.; Zhang, T.; Dai, J.; Xu, K. Switching dynamics of dissipative cnoidal waves in dual-coupled microresonators. *Opt. Express* **2021**, *29*, 42369–42383. [CrossRef]

23. Tikan, A.; Riemensberger, J.; Komagata, K.; Hönl, S.; Churaev, M.; Skehan, C.; Guo, H.; Wang, R.N.; Liu, J.; Seidler, P.; et al. Emergent nonlinear phenomena in a driven dissipative photonic dimer. *Nat. Phys.* **2021**, *17*, 604–610. [CrossRef]

24. Tikan, A.; Tusnin, A.; Riemensberger, J.; Churaev, M.; Ji, X.; Komagata, K.N.; Wang, R.N.; Liu, J.; Kippenberg, T.J. Protected generation of dissipative Kerr solitons in supermodes of coupled optical microresonators. *Sci. Adv.* **2022**, *8*, eabm6982. [CrossRef] [PubMed]

25. Helgason, Ó.; Girardi, M.; Ye, Z.; Lei, F.; Schroder, J.; Torres-Company, V. Surpassing the nonlinear conversion efficiency of soliton microcombs. *Nat. Photonics* **2023**, *17*, 992–999. [CrossRef]

26. Helgason, Ó.B.; Arteaga-Sierra, F.R.; Ye, Z.; Twayana, K.; Andrekson, P.A.; Karlsson, M.; Schröder, J.; Torres-Company, V. Dissipative solitons in photonic molecules. *Nat. Photonics* **2021**, *15*, 305–310. [CrossRef]

27. Yuan, Z.; Gao, M.; Yu, Y.; Wang, H.; Jin, W.; Ji, Q.-X.; Feshali, A.; Paniccia, M.; Bowers, J.; Vahala, K. Soliton pulse pairs at multiple colours in normal dispersion microresonators. *Nat. Photonics* **2023**, *17*, 977–983. [CrossRef]

28. Stone, B.; Rukh, L.; Colación, G.; Drake, T. Enhanced thermal stability of soliton states in coupled Kerr microresonators. In Proceedings of the Frontiers in Optics Laser Science 2023, Tacoma, DC, USA, 9–12 October 2023; Optica Publishing Group: Washington, DC, USA, 2023; p. JTu4A.44.

29. Xu, X.; Jin, X.; Lu, Y.; Gao, H.; Cheng, J.; Yu, L. Stability analysis of the optical field and spectrum characteristics inside the dual coupled microcavities. *J. Opt.* **2020**, *22*, 115501. [CrossRef]

30. Xue, X.; Xuan, Y.; Wang, H.; Wang, P.H.; Wang, J.; Leaird, D.E.; Qi, M.; Weiner, A.M. Normal-dispersion microcombs enabled by controllable mode interactions. *Laser Photon. Rev.* **2015**, *9*, L23–L28. [CrossRef]

31. Calvo-Salcedo, A.F.; Tu, C.; Gonzalez, N.G.; Menyuk, C.; Jaramillo-Villegas, J.A. Simulation of Electrically-Controlled Mode Interaction for Adiabatic and Deterministic Single Soliton Generation. In Proceedings of the OSA Advanced Photonics Congress IPRSN, Virtual Event, 26–30 July 2021; Optica Publishing Group: Washington, DC, USA, 2021; p. JTu1A.5. [CrossRef]

32. Xuan, Y.; Liu, Y.; Varghese, L.T.; Metcalf, A.J.; Xue, X.; Wang, P.H.; Han, K.; Jaramillo-Villegas, J.A.; Noman, A.A.; Wang, C.; et al. High-Q silicon nitride microresonators exhibiting low-power frequency comb initiation. *Optica* **2016**, *3*, 1171–1180. [CrossRef]

33. Kim, S.; Han, K.; Wang, C.; Jaramillo-Villegas, J.A.; Xue, X.; Bao, C.; Xuan, Y.; Leaird, D.E.; Weiner, A.M.; Qi, M. Dispersion engineering and frequency comb generation in thin silicon nitride concentric microresonators. *Nat. Commun.* **2017**, *8*, 372. [CrossRef]

34. Liu, Y.; Xuan, Y.; Xue, X.; Wang, P.H.; Chen, S.; Metcalf, A.J.; Wang, J.; Leaird, D.E.; Qi, M.; Weiner, A.M. Investigation of mode coupling in normal-dispersion silicon nitride microresonators for Kerr frequency comb generation. *Optica* **2014**, *1*, 137–144. [CrossRef]